35th Fluid Dynamics Meeting,Toronto, Canada, June 2005

Assessment of STBLI DNS Data and Comparison against Experiments

Minwei Wu[*], Ellen M. Taylor[†], and M. Pino Martín[‡]
Department of Mechanical and Aerospace Engineering
Princeton University, Princeton, NJ

The direct numerical simulation data of a Mach 2.9 turbulent boundary layer flowing over a 24-degree compression ramp are assessed. A summary of the flow features and the comparison of the simulation data against experiments are given. Of main interest are discrepancies found in the wall-pressure distribution. The flow characteristics of the separation shock foot are studied to better understand the wall-pressure prediction, and the effect of the numerical shock capturing technique on the data is considered.

I. Introduction

In previous work,[1,2,3,4] we performed detailed experiments and direct numerical simulations (DNS) of shock/turbulent boundary layer interaction (STBLI) under the same flow conditions in order to support the development of accurate computational fluid dynamics (CFD) models. We identified three canonical configurations and their corresponding flow conditions, so that the flow conditions are within the numerical and experimental capabilities. We built experimental models and developed accurate and efficient procedures to initialize the numerical flow fields and simulate the STBLI at the same conditions as the experiments. In addition, preliminary simulations and experiments were conducted at two Mach numbers, Mach 3 and 8, and at Reynolds numbers ranging from 2400 to 3400. Figure 1 shows the selected STBLI configurations, including a compression corner, incident shockwave and sharp-fin induced interaction cases. We have not performed any simulations on the sharp-fin induced case, however the experimental data have been reported.[4]

The numerical/experimental collaboration has been challenging, but also fruitful. We have found remarkable agreement between the preliminary numerical data and existing experimental data (in turbulence structure angles, velocity profiles, mass flux amplification, and skin friction coefficient), yet we have also found important discrepancies (particularly the lack of a plateau in the wall pressure distribution and the size of the separation bubble). The degree of agreement and disagreement between the experiments and simulations is consistent for the compression corner and incident shockwave cases. In spite of the discrepancies with the experimental data for each individual configuration, the expected similarities between the compression corner and reflected wave configurations, as observed experimentally,[5,6] are found in the DNS data. Namely, the 24° compression corner produces the same series of compression interactions at separation and reattachment as the incident shock case with initial 12° deflection, and the overall pressure change is the same with the surface pressure distributions being nearly identical. Thus, the cause for the deficiencies in the DNS data appears to be the same for both interaction cases.

In this paper, we assess the deficiencies of the DNS data and their possible source in the context of the compression corner. The paper is organized as follows. The numerical method, flow and boundary conditions are described in Section II. A summary of the characteristics for the compression corner interaction and the comparison of the DNS against experimental data are given in Section III. Section IV describes discrepancies in the wall-pressure distribution and the flow characteristics of the separation shock foot. The effect of the

---

[*] Student Member AIAA

[†] Student Member AIAA

[‡] Member AIAA `pmartin@princeton.edu`

	Re_θ	θ (mm)	δ^* (mm)	C_f	δ_{99} (mm)
Experiment[4]	2397	0.428	2.36	0.00225	7.24
DNS A[2,3]	2400	0.850	2.65	0.00204	6.35
DNS B	2550	0.450	2.10	0.00197	7.50

Table 1. Conditions for the incoming turbulent boundary layer at Mach 2.9.

numerical shock capturing technique on the wall-pressure distribution and on the existence of a plateau are explored in Section V. Conclusions are given in Section VI.

II. Numerical method, boundary conditions and flow conditions

A 3rd-order, bandwidth- and dissipation-optimized WENO (Weighted Essential Non-oscillatory) scheme[7] is used to approximate the convective flux terms in the governing equations. This scheme has been designed for high bandwidth and low dissipation, while being a shock capturing scheme. A 4th-order standard central scheme is used to compute the viscous terms. As for the time integration, we use a 3rd-order low-storage Runge-Kutta method.

Using the WENO scheme, there is no need to know the location of the shock patterns *a priori* and to perform manual shock fitting at known shock locations. Thus, given a configuration, a sensible grid spacing, and provided that the inflow conditions are accurate, a robust WENO method would provide the correct solution to any general type of shock interaction.

A. Initial conditions

Prescribing and controlling the initial flow conditions computationally has received a great deal of attention. The initialization procedure is sketched in Fig. 2. The first step is to develop an initial flow field for the incoming boundary layer. A RANS calculation is performed to get the mean flow quantities. Then the fluctuations are obtained by transforming the turbulence of a Mach 0.3 turbulent boundary layer DNS data to that of the desired Mach number using Morkovin's scaling laws and the strong Reynolds analogy (SRA). We run the incoming boundary layer during a DNS until it reaches a statistically stationary state. After that, we interpolate the flow field of the incoming boundary layer onto the inlet for the STBLI case. Then, the last profile of the inlet is copied to the rest of the computational domain to initialize the flow field. The initialization procedure for the STBLI is discussed further by Martin et al[1] and details about the initial transformations for the incoming boundary layer data can be found in Martin's 2003 and 2004 papers.[8,9] This initialization procedure allows for fast turn-around of the initial domain into a physical state where we begin gathering statistics.

B. Boundary conditions

To obtain a continuous incoming turbulent flow and maintain the upstream inflow conditions, a rescaling method for compressible flows was developed by Xu and Martin.[10] The main concept of the rescaling method is to take a profile at some place downstream of the computational domain and rescale it using scaling laws, then inserted it at the inlet to get continuous inflow data.[10] At the outlet, we use the sponge layer technique[11] to minimize flow reflections. At the top boundary, we use supersonic exit boundary conditions. In the spanwise direction, periodic boundary conditions are used. The wall boundaries are set to be isothermal, with the wall temperature being prescribed to roughly the adiabatic wall temperature. The combination of a fully parallel code implementation, efficient initialization procedures, and effective inflow boundary conditions allows for reduced turn-around of DNS statistics.

Case	L_x/δ	L_y/δ	L_z/δ	N_x	N_y	N_z
Ramp	13	2	4.5	412	128	96
Reflect 1	15.8	2	4.5	412	128	128
Reflect 2	15	2	7.4	412	128	96

Table 2. Domain size and number of grid points for the DNS data, where x, y and z correspond to the streamwise, spanwise and wall-normal directions, respectively.

C. Flow conditions, grid and statistical sample size

In this paper, we work with the compression corner data.[2,3,4] The incoming Mach number is 2.9, the Reynolds number based on the momentum thickness is $Re_\theta = 2400$ to 2550, and the turning angle is 24 degrees, so that the interaction causes the flow to separate. The properties of the incoming boundary layer for the experiments and simulations are listed in Table 1. Two simulation conditions are given, where simulation A was performed prior to the experiments and the freestream density was one order of magnitude different than that in the wind tunnel, thus leading to a slightly different wall-temperature condition. No significant differences have been observed in the data between simulations A and B.

Numerical errors associated with the discrete evaluation of the Jacobian matrices might be amplified through the simulation. Therefore, we use analytical transformations to generate the grids and to minimize these errors. For the compression corner case, the transformations are chosen to make the grid clustered near the wall in the wall-normal direction and near the corner along the streamwise direction. In the spanwise direction, the grid is equally spaced. Figure 3a shows a sample grid for the compression corner. More details can be found in Martin *et al.*[1] and Wu & Martin.[2] Figure 3b shows the computational domain for the compression corner case. The length in the wall-normal direction is about 4.5δ, where δ is the thickness of the incoming boundary layer. In the spanwise direction, the domain size is 2δ. The corner is 7δ away from the inlet. The length along the ramp is 6δ. The dashed parallelogram indicates the location for the rescaling station, which is at 4δ downstream of the inlet. We have verified that changing the rescaling location further downstream[2] or increasing the size of the computational domain in the spanwise direction[3] has no effect on the resulting data. The computational domain size and the number of grid points are listed in Table 2. The maximum and minimum grid spacings in the streamwise direction are 15.5 and 7.2 wall units, respectively. In the spanwise direction, the grid spacing is 4.4 wall units. In the wall-normal direction, there are 21 grid points within 10 wall units, and the spacing at the boundary layer edge is 5% of the boundary layer thickness.

For the conditions chosen, the frequency of oscillation for the separation shock is of the order of U_∞/δ,[2] where U_∞ is the freestream velocity. We gather 80 statistical samples within 40 δ/U_∞ time scales. This takes three days in the CROCCO Lab computing facility. Doubling the number of statistical samples and time scales does not change the simulation results.

III. Compression corner case

In this section, we review the flow characteristics of STBLI for the compression corner configuration as observed in experiments. In addition, the comparison of the DNS data against the experimental ones is revisited.[3]

A. Flow characteristics

The compression corner interaction is one of the simplest cases of STBLI that occur in internal and external vehicle flows. This configuration has been extensively studied experimentally, where some exemplary references are given within.[12,13,14,15,16,17,4] The previous research covers a wide range of turning angles and Reynolds numbers, but the lowest Reynolds number reported prior to year 2005 was $Re_\theta = 23{,}000$.[12] Also prior to the experimental work of Bookey *et al*,[4] the upper Mach number was limited to about 5.[18] At higher Mach numbers, the interaction tends to be laminar. See, for example, Verma (2003)[19] for a compression corner study at Mach 9. Very little information is available on turbulent interactions at high Mach number. The recent experiments of Bookey *et al*[4] include data at DNS-accessible Reynolds numbers for various configurations. Their studies of the compression corner were at Mach 2.9 with 24° deflection angle and $Re_\theta = 2400$, and at Mach 8 with 8° deflection angle and $Re_\theta = 3500$.

The pressure gradient imposed by the shock can cause the flow to separate in the vicinity of the corner location, and at Mach 2.9 the flow is on the verge of separation with a corner angle of 16° (called incipient separation). At 24° and in the high Reynolds number range (Re_θ of about 68,000), the time-averaged region of separation spans about 2δ, starting approximately 1.2δ ahead of the corner and reattaching at about 0.8δ downstream of the corner. Near the line of separation, compression waves merge into a well-defined separation shock, and a second shock forms near the line of attachment.[20] Figure 4 illustrates the shock system in a compression corner configuration with increasing compression angle. The corresponding wall pressure distribution shows an inflection point or plateau in the region of separation, as shown in Figure 5. Further downstream, the wall-pressure eventually recovers to the inviscid oblique-shock value, but the point where this occurs is located farther downstream with increasing compression angle.[12] For the 24° case, the inviscid value is not recovered before the end of the experimental model is reached, nearly eight boundary layer thicknesses downstream of the corner.[12]

A measure of the upstream influence is the distance from the corner at which the shock presence is first felt. A measure of the streamwise interaction extent is the separation length, being the distance between the separation and reattachment points. These characteristic lengths are determined from time-averaged measurements, and they vary with time due to the highly unsteady motion of the separation shock. The distance over which the separation shock moves increases with turning angle, and at 24° and Re_θ of about 68,000, the shock moves about 0.5δ.[17] The frequency is typically an order of magnitude lower than any characteristic turbulence frequencies, and of the order of 1 kHz. Thus, the frequency and scale of the shock motion are needed to fully characterize the interaction.

The influence of the compression on the turbulence is an enhanced mixing due to the formation of large-scale eddies[13] as the incoming boundary layer is driven out of equilibrium. The boundary layer mean flow recovery distance increases with increasing interaction strength.[14, 17, 16, 13] The turbulence levels are strongly amplified across the shock system, and it is found[17] that at Mach 2.9 the mass-flux fluctuations increased by a factor of about 4.8 with a 24° turning angle. The flow distortion is also seen in the heat transfer. For example, it is found that the Reynolds analogy factor increased by a factor of 3 through a 16° interaction, and showed little sign of relaxation downstream of the corner.[21]

The preliminary experiments of Bookey *et al.*[4] at $Re_\theta = 2400$ allow studying the effect of Reynolds number by comparing the data with the high Reynolds number ones at Re_θ of about 68,000.[17, 12, 15, 22] Figure 6 shows the wall-pressure distribution for the compression corner interaction at high and low Reynolds numbers. We observe that the length of the pressure plateau increases with decreasing Reynolds number. Thus, the size of the separation bubble and the location of detachment are Reynolds number dependent. In addition, the boundary layer downstream of the interaction recovers to equilibrium more slowly for the lower Reynolds number data.

B. DNS data and comparison against experiments

The DNS statistics for the 24° compression corner interaction at Mach 2.9 and Re_θ of 2400 have been presented previously[2, 3] and are briefly summarized here. The flow conditions for the incoming boundary layer are given in Table 1. Figure 7 shows the Van-Driest transformed velocity profile for the incoming boundary layer. In the viscous sublayer, we see good agreement with the expected velocity distribution. In the logarithmic region, there is good comparison with the experimental data at the same Reynolds number, except in the near wall region where the velocity measurement in the experiment is not expected to be accurate because of probe resolution issues. The structure of the incoming boundary layer may be described using the two-dimensional density correlations. Figure 8 shows both correlations from the experiment and DNS. The correlations have the same shape and angle, indicating that the structures inside the incoming boundary layer in the experiment and DNS are similar.

Figure 9 plots a sequence of $|\nabla\rho|$ contour for the compression ramp case to illustrate the shock unsteady motion. Time increases from (a) to (f). The interval between each frame is about $2\delta/U_\infty$. Figure 10 shows filtered Rayleigh scattering images from the experiments and density contour plots from DNS data. We observe similar structures in the incoming boundary layers and near the interaction regions.

Figure 11 shows the Van-Driest transformed velocity profiles at different streamwise locations for the DNS.

Open and closed symbols indicate the locations upstream and downstream of the interactions, respectively. There is a characteristic 'dip' in the log region for the mean velocity profile downstream of the interaction. This is consistent with the experimental observations of Smits and Muck[14] at Mach 2.9 and $Re_\delta = 1.64 \times 10^6$.

Figure 12 plots the mass flux turbulence intensity upstream and downstream of the interaction for the DNS. The mass flux turbulence intensity is greatly amplified through the interaction. Downstream of the interaction, the maximal value of the mass flux turbulence intensity is amplified by a factor of about 5. Figure 13 shows the comparison of the mass flux turbulence intensity given by DNS and experimental data upstream and downstream of the interaction. The discrepancy between the simulation and experiment is about 20%, which is considered good agreement because it is within the experimental error. The peaks of the mass flux turbulence intensity in the experiment and DNS are also found in good agreement. The amplification factor is about 4.8 for Selig's experiment,[23] which is consistent with the DNS data.

Figure 14 shows the skin friction coefficient from the DNS data. From this figure, we observe that the average size of the separation is about 2.1δ. Zheltovodov *et al.*[24] found a correlation for the separation length as a function of the Reynolds number

$$\frac{L_{\rm sep}}{L_{\rm c}} = f(Re_\delta), \tag{1}$$

where

$$L_{\rm c} = \frac{\delta}{M_\infty^3}\left(\frac{P_2}{P_{\rm pl}}\right)^{3.1} \tag{2}$$

with P_2 as the inviscid pressure downstream of the interaction and $P_{\rm pl}$ is the plateau pressure computed using the empirical formula given by Zukoski[25]

$$P_{\rm pl} = P_\infty\left(\frac{1}{2}M_\infty + 1\right), \tag{3}$$

and $f(Re_\delta)$ is plotted in Fig. 15. According to these empirical formulas, the size of the separation zone for the 24° compression corner at $Re_\theta = 2400$ is between 3.3δ and 4.6δ, which is underpredicted by the DNS data. By comparison, the skin friction distribution and the flow visualization data at Re_θ of 2400 shows a separation length of about 2δ

Figure 16 shows the wall pressure distribution. The DNS data agree well with the experimental data downstream of the interaction. As observed experimentally,[12] the inviscid pressure ($P_{\rm w}/P_\infty$ about 4.5) is not recovered within eight boundary layer thickness downstream of the interaction. There is a noticeable difference between numerical and experimental data inside the separation region, upstream of the corner. In all the experimental data sets, including low and high Reynolds numbers, there is a plateau in the wall pressure distribution shortly after the wall pressure rises. In contrast, this feature is not found in the DNS data. This discrepancy is discussed in more detail in the next section.

IV. Discrepancies between DNS and experimental data

We find that the structure angle and the skin friction coefficient for the incoming boundary layer given by the DNS are in good agreement with the experimental data. In addition, the velocity profiles and the mass-amplification factor are also in good agreement. We find that the turbulence structures within the interaction are qualitatively similar to the experimental ones. In contrast, the size of the separation bubble and the wall pressure distribution are not accurately reproduced. These are important discrepancies because the heat transfer and the detailed flow physics are affected by the separation shock and the recirculating bubble. In this section, we study the details of these discrepancies.

A. Signature of the shock interaction

As mentioned in Section III, the incipient angle of separation for a Mach 3 interaction is about 16° independently of Reynolds number.[20] Thus, at compression angle of 16° or higher, a separation shock forms upstream of the so called "inviscid" shock. The resulting shock system is λ-shaped. The signature of the shock system is an inflection point and a plateau region in the wall-pressure distribution, which are missed in the present DNS data.

Figure 17 plots time-averaged Mach number contours and streamlines for the DNS[3] and experimental[20] data with $Re_\theta = 2400$ and 68,000, respectively. The separation region is identified by the Mach zero contour line, which is very close to the wall for the DNS data and therefore not visible. Thus, the DNS separation region is very thin, less than 1% of the boundary layer thickness. Comparing the DNS and experimental data, we observe that the location of the sonic line matches in the DNS and experiments. However, the separation region extends a larger wall-normal distance in the high Reynolds number experiment. From figures 15 and 16, reducing the Reynolds number results in a larger streamwise extent of the separation region and a stronger pressure gradient at the onset of separation. Thus, reducing the Reynolds number results in an overall increase of the separation size in the streamwise and wall normal directions, and we should expect a larger wall-normal extent of the separation bubble in the DNS. Figure 18 shows the streamlines for the DNS. We observe the concave pattern, indicating that the flow is compressed gradually. The resulting pressure distribution is quite different from that seen in the experiment, where the initial pressure rise is abrupt, and a plateau region is seen to extend over a considerable distance.

As the shock penetrates into the boundary layer, it is diffused and weakened. In the near wall interaction region, the Mach number changes gradually. A possible explanation for the discrepancy of the wall pressure distribution between the experimental and numerical data might be as follows. The strength of the shock at the shock foot is weaker for the numerical data. In turn, the rise in pressure will be more gradual than that in the experiments. The suggested shock patterns and pressure variations are sketched in Figure 19. For the experiment, there are two strong compressions inside the interaction region. Thus, the wall pressure has two distinct steps, connected by a plateau region. For the simulation data, however, the flow turns gradually in a concave pattern. Therefore a compression fan (instead of a shock) is formed, which converges into the shock at a distance from the wall that is greater than that seen in the experiments.

Thus, the first distinct compression is not observed in the current numerical data. It is interesting to note that the DNS data of Adams[26] at Re_θ=1685 also show no plateau in the wall pressure at 18° compression angle.

B. Flow characteristics of the separation shock foot for the DNS

Figure 20a plots contours of entropy for an instantaneous flow field, showing the location of the shock furthest upstream and the penetration of the shock deep into the boundary layer. Figure 20b plots a numerical schlieren for the same instant. The sonic line, the Mach zero line delineating the separation zone, and the expected and the DNS prediction of the shock-foot location (expected value upstream) are also plotted for reference. The expected location is based on choosing the wall-normal distance at the sonic point and at the streamwise location where the onset of separation is given by the zero-Mach line. At this location, we observe that the shock foot should penetrate as deep as the viscous sublayer. In contrast, the DNS predicts the shock foot further downstream and further away from the wall. Figure 21 plots the profile of the normalized magnitude of velocity fluctuations at the expected shock-foot location. The symbol indicates the sonic point, the location of the shock foot. The expected shock foot occurs in the viscous sublayer, near the peak of turbulence intensity. We hypothesize that, for the local shock-foot conditions, the turbulence intensities are stronger than the shock-jump conditions, and the shock-capturing technique is not detecting the shock foot. This hypothesis is assessed in the following section.

V. Effect of WENO adaption mechanism

In this section, we briefly describe the shock-capturing method. We assess the sensitivity of the shock-capturing mechanism under the flow conditions found at the shock-foot, and we study possible ways to enhance the shock-capturing sensitivity.

A. WENO adaption mechanism

The WENO method was first designed by Liu *et al.*[27] and Jiang & Shu[28] for robust shock-capturing while ensuring high-order accuracy away from discontinuities. The final derivative approximation is given as a weighted sum of a number of candidate approximations, where the weights depend on local data. Thus, in smooth data, the technique leads to an "optimal stencil". In contrast to non-smooth data, the stencil that includes a discontinuity is discarded. Jiang & Shu,[28] modified the original WENO technique to maximize the order of accuracy. Given the large number of frequencies in turbulent flows, the frequency-resolving efficiency of the numerical scheme is crucial to achieve accurate results. Thus, Weirs & Candler[7] further modified the WENO scheme to maximize bandwidth and minimize dissipation. In our simulations, we employ the final bandwidth- and dissipation-optimized WENO scheme.[7, 29]

We summarize the details of the bandwidth- and dissipation-optimized WENO method in the context of the scalar, one-dimensional advection equation,

$$\frac{\partial u}{\partial t} + \frac{\partial}{\partial x} f\left(u\right) = 0 \tag{4}$$

If the spatial domain is discretized such that $x_i = i\Delta$, where Δ is the grid spacing and $u_i = u\left(x_i\right)$, Eqn. (4) may be cast into the semidiscretized form

$$\frac{du_i}{dt} = -\frac{1}{\Delta}\left(\hat{f}_{i+\frac{1}{2}} - \hat{f}_{i-\frac{1}{2}}\right) \tag{5}$$

where $\hat{f}_{i+1/2}$ is a numerical approximation of $f\left(u\left(x_{i+1/2}\right)\right)$. In order to ensure stability, procedures that approximate $f\left(u\right)$ generally split it into $f^{+}\left(u\right)$ and $f^{-}\left(u\right)$, where these fluxes have strictly non-negative and strictly non-positive derivatives, respectively. WENO schemes compute $\hat{f}^{+}_{i+1/2}$ through interpolating polynomials on a number of r candidate stencils. In the modified WENO method, each stencil contains r grid points. The one fully upwinded stencil ranges from $(i-r+1)$ to i, the one fully downwinded stencil ranges from $(i+1)$ to $(i+r)$, and the other stencils fall in between these two extremes. This collection of stencils is symmetric about the point $\left(i+\frac{1}{2}\right)$ to minimize dissipation. Thus, the numerical representation of the flux is given by

$$\hat{f}^{+}_{i+\frac{1}{2}} = \sum_{k=0}^{r} \omega_k q^r_k \ , \tag{6}$$

where q^r_k is the candidate flux at $(j+1/2)$ and and ω_k are the optimal weights for each candidate flux. These are given by

$$q^r_k = \sum_{l=0}^{r} a^r_{k,l} f(u_{j-r+1+k+l}) \qquad w_k = \frac{C^r_k/(\epsilon + IS_k)^p}{\sum_{k=0}^{r} c^r_k/(\epsilon + IS_k)^p} \ , \tag{7}$$

where $a^r_{k,l}$ are the optimized coefficients, C^r_k are the ideal weights for the candidate fluxes, and IS_k is the smoothness measurement, which is given by

$$IS_k = \sum_{m=1}^{r-1} \int_{x_{j-1/2}}^{x_{j+1/2}} (\Delta x)^{2m-1} \left(\frac{\partial^m q^r_k}{\partial x^m}\right)^2 dx \tag{8}$$

Increasing the coefficient p in Eqn. (7) gives more sensitivity to non-smooth data. In completely smooth regions, every stencil is equally desirable, and the weights revert to the optimal weights C_k. Because the total number of data points available to the modified WENO algorithm is $2r$, its maximum order of accuracy is also $2r$. In practice, the weight of the fully downwinded stencil ω_r is artificially constrained to be no greater than the least of the others so that adverse stability effects are avoided. Figure 22 shows a sketch of the candidate stencils and fluxes for r=3, which is used in our DNS of STBLI.

B. Shock-capturing sensitivity at the shock foot

Using DNS, Taylor *et al.*[30] studied the local adaption and dissipation properties of the bandwidth- and dissipation-optimized WENO method on decaying isotropic turbulence at various turbulent Mach numbers. They presented a procedure for the identification of shock-containing and smooth regions, where the WENO adaption mechanism is engaged and reverted to the linear optimal stencil, respectively. In this context it is possible to study the sensitivity of the WENO method to adapt in non-smooth regions. In this section, we perform exploratory numerical studies of the WENO adaption mechanism in isotropic turbulence and in the compression corner STBLI.

As a numerical experiment, we run a DNS of two-dimensional decaying isotropic turbulence and study the adaption mechanism at the conditions found in the expected shock foot location of the STBLI. Near the shock foot, the local Mach number is close to one, thus the strength of the shock is weak. For the numerical experiment in isotropic turbulence at the same local conditions of the STBLI shock foot, we assume that the shocklets that form are of similar strength to that of the shock foot. In the isotropic turbulence simulation, shocklets are identified using the shock-identification mechanism of Taylor *et al.*[30] In this way, instantaneous streamlines across shocklets are identified. Then, using indexes of local adaption,[30] we investigate the sensitivity of the WENO adaption mechanism across the shocklets and, therefore, its effectiveness identifying such weak shocks.

For the numerical experiment in isotropic turbulence, Figure 23 plots density and pressure along instantaneous streamlines across a shocklet of common strength for the conditions chosen, where the shock is centered along the x axis. The flow conditions match those at the expected and DNS-predicted shock-foot locations in the incoming turbulent boundary layer, where the corresponding turbulent Mach numbers are $M_t = 0.2$ and 0.5, respectively. The jump in the thermodynamic variables indicates shocks of strength $M = 1.03$ and 1.21 for the $M_t = 0.2$ and 0.5, respectively. An index of the local adaption is the nonlinearity index, NI, which is also plotted in the figure. For third-order of accuracy, the numerical values of NI range in [0:3.5], where NI increases with increasing non-smoothness of the data. For M_t=0.2, we observe that the value of NI is not large, relative to the values found in the smooth data (at $x = -20$, for example). This result suggests that such shock strength might not be identified in a STBLI simulation either. In contrast, we observe relatively large values of NI for the $M_t = 0.5$ case.

From Eqn. (7), increasing p leads to higher sensitivity of non-smooth data. We have investigated the effect of increasing p in the DNS. For isotropic turbulence, Fig. 24 shows that increasing p allows for the shock-capturing of weak-strength shocklets (Figure 24a), while not enhancing the dissipation of the numerical scheme, see Figures 25a and 25b. For isotropic turbulence, values greater than $p = 1.4$ result in numerical instabilities.

Figure 26 plots the wall-pressure distribution for the DNS of STBLI varying p. For $p = 2$, we observe the presence of an inflection point at $P = P_{\mathrm{pl}}$, which is 2.5 according to the experimental data, the theory,[25] and the DNS data. For $p = 3$, we observe the same inflection point at $P = P_{\mathrm{pl}}$, as well as a second inflection point further upstream. These are subtle, yet promising results that give evidence of the data-dependence on p. However, further increasing p causes numerical instabilities. Additional ways to increase the sensitivity of the smoothness measurement parameter for the WENO scheme are being considered.[31, 32]

VI. Conclusions

In this paper, we review the direct numerical simulation data of a Mach 2.9 turbulent boundary layer over a 24° compression corner. The flow characteristics are described by summarizing the findings in experiments for Reynolds numbers in the range of $Re_\theta = 2400$ to 68,000. The DNS data are then compared against experiments. It is found that the velocity profile, the turbulence structure and the skin friction of the incoming boundary layer are accurately predicted. The turbulence structures within the interaction region are qualitatively similar to those found in experiments at the same conditions. The Van-Driest transformed velocity profiles resemble the experimental ones through the interaction. The expected turbulence amplification factor is predicted, and the mass flux turbulence intensity profiles upstream and downstream of the interaction are predicted within the experimental uncertainty. The wall pressure recovery downstream of the interaction is well predicted. However, the size of the separation bubble is underpredicted, and the plateau in the wall-pressure distribution is not predicted.

It is also found that the present formulation of the shock-capturing technique is not sensitive to weak-shock strengths (of the order of those found near the shock foot), and a preliminary investigation of the stencil-adaption mechanism for the numerical method and its effectiveness has been presented. Increasing the sensitivity of the stencil-adaption mechanism using parameter p does not significantly change the STBLI data. Additional ways to formulate the smoothness measurement for the shock-capturing scheme are being considered, as well as other possible causes for the disagreement between the DNS and experimental data.[31, 32]

VII. Acknowledgments

This work is supported by the Air Force Office of Scientific Research under grant AF/F49620-02-1-0361.

References

[1] Martin, M., Xu, S., and Wu, M., “Preliminary work on DNS and LES of STBLI,” *AIAA Paper No. 03-3964*, 2003.

[2] Wu, M. and Martin, M., "Direct Numerical Simulation of Shockwave/Turbulent Boundary Layer Interactions," *AIAA Paper No. 2004-2145*, 2004.

[3] Wu, M., Bookey, P., Martin, M., and Smits, A., "Analysis of Shockwave/Turbulent Boundary Layer Interaction using DNS and Experimental Data," *AIAA Paper No. 2005-0310*, 2005.

[4] Bookey, P., Wu, M., Smits, A., and Martin, P., "New Experimental Data of STBLI at DNS/LES Accessible Reynolds Numbers," *Extend abstract submitted to the 43rd AIAA Aerospace Sciences Meeting and Exhibit. Reno, N*, January 2005.

[5] Green, J., "Interaction Between Shockwaves and Turbulent Boundary Layers," *Progress in Aerospace Sciences*, Vol. 11, 1970.

[6] Shang, J., Hankey, J. W., and Law, C., "Numerical simulation of shockwave/turbulent boundary layer interaction," *AIAA Journal*, Vol. 14, 1976, pp. 1451–1457.

[7] Weirs, G. and Candler, G., "Optimization of Weighted ENO Schemes for DNS of Compressible Turbulence," *AIAA Paper No. 97-1940*, 1997.

[8] Martin, M., "Preliminary DNS Database of Hypersonic Turbulent Boundary Layers," *AIAA Paper No. 03-3464*, 2003.

[9] Martin, M., "Hypersonic Turbulent Boundary Layers: Understanding the Physics to Perform Accurate Complex Simulations," *AIAA Paper No. 2004-2337*, 2004.

[10] Xu, S. and Martin, M. P., "Inflow Boundary Conditions for Compressible Turbulent Boundary Layers," *AIAA Paper No. 03-3963*, 2003.

[11] Adams, N., "Direct numerical simulation of turbulent compression ramp flow," *Theoretical and Computational Fluid Dynamics*, Vol. 12, 1998, pp. 109–129.

[12] Settles, G., Fitzpartrick, T., and Bogdonoff, S., "Detailed Study of Attached and Separated Compression Corner Flowfields in High Reynolds Number Supersonic Flow," *AIAA Journal*, Vol. 17, No. 6, 1979, pp. 579–585.

[13] Kuntz, D., Amatucci, V., and Addy, A., "Turbulent boundary layer properties downstream of the shockwave/boundary-layer interaction," *AIAA Journal*, Vol. 25, 1987, pp. 668–675.

[14] Smits, A. and Muck, K., "Experimental study of three shock wave/turbulent boundary layer interactions," *J. Fluid Mech.*, Vol. 182, 1987, pp. 291–314.

[15] Dolling, D. and Murphy, M., "Unsteadiness of the Separation Shock Wave in a Supersonic Compression Ramp Flowfield," *AIAA Journal*, Vol. 21, No. 12, 1983.

[16] Ardonceau, P., "The structure of turbulence in a supersonic shockwave/boundary layer interaction," *AIAA Journal*, Vol. 22, No. 9, 1984, pp. 1254–1262.

[17] Selig, M., Muck, K., Dussauge, J., and Smits, A., "Turbulent Structure in a Shock Wave/Turbulent Boundary-Layer Interaction," *AIAA Journal*, Vol. 27, 1989, pp. 862–869.

[18] Erengil, M. and Dolling, D., "Unsteady wave structure near separation in a Mach 5 compression ramp interaction," *AIAA Journal*, Vol. 29, No. 5, 1991, pp. 728–735.

[19] Verma, S., "Experimental study of flow unsteadiness in a Mach 9 compression ramp interaction using a laser schlieren system," *Measurements in Science and Technology*, Vol. 14, 2003, pp. 989–997.

[20] Settles, G., Vas, I., and Bogdonoff, S., "Details of a shock-separated turbulent boundary layer at a compression corner," *AIAA Journal*, Vol. 14, No. 12, 1976, pp. 1709–1715.

[21] Evans, T. and Smits, A., "Measurements of the Heat Transfer in a Shock Wave Turbulent Boundary Layer Interaction," *Experimental Thermal and Fluid Science*, Vol. 12, 1996, pp. 87–97.

[22] Dolling, D. and Or, C., "Unsteadiness of thehock wave structure in attached and separated compression corner flow fields," *AIAA Paper No. 1983-1715*, 1983.

[23] Selig, M. S., *Unsteadiness of Shock Wave/Turbulent Boundary Layer Interactions with Dynamic Control*, Ph.D. thesis, Princeton University, 1988.

[24] Zheltovodov, A. and Schülein, E. Horstman, C., "Development of separation in the region where a shock interacts with a turbulent boundary layer perturbed by rarefaction waves," *Journal in Applied Mechanics and Technical Physics*, Vol. 34, No. 3, 1993, pp. 346–354.

[25] Zukoski, E., "Turbulent boundary layer separation in front of a forward facing step," *AIAA Journal*, Vol. 5, No. 10, 1967, pp. 1746–1753.

[26] Adams, N., "Direct numerical simulation of turbulent boundary layer along a compression ramp at M=3 and Re_θ=1685," *J. Fluid Mech.*, Vol. 420, 2000, pp. 47–83.

[27] Liu, x.-D., Osher, S., and Chan, T., "Weighted essentially non-oscillatory schemes," *Journal of Computational Physics*, Vol. 115, 1994, pp. 200–212.

[28] Jiang, G.-S. and Shu, C.-W., "Efficient implementation of weighted ENO schemes," *Journal of Computational Physics*, Vol. 126, 1996, pp. 202–228.

[29] Weirs, V. G., *A numerical method for the direct simulation of compressible turbulence*, Ph.D. thesis, University of Minnesota, December 1998.

[30] Taylor, E., Martin, M., and Weirs, G., "Local adaption and dissipation properties of a weighted essentially non-oscillatory scheme," *AIAA Paper No. 2004-2706*, 2004.

[31] Wu, M. and Martin, M., "Analysis of shockwave/turbulent boundary layer interaction using DNS data," *Extended abstract submitted to the 44th AIAA Aerospace Sciences Meeting and Exhibit*, 2006.

[32] Taylor, E. and Martin, M., "Characterization of local-stencil adaption for a weighted essentially non-oscillatory scheme," *Extended abstract submitted to the 44th AIAA Aerospace Sciences Meeting and Exhibit*, 2006.

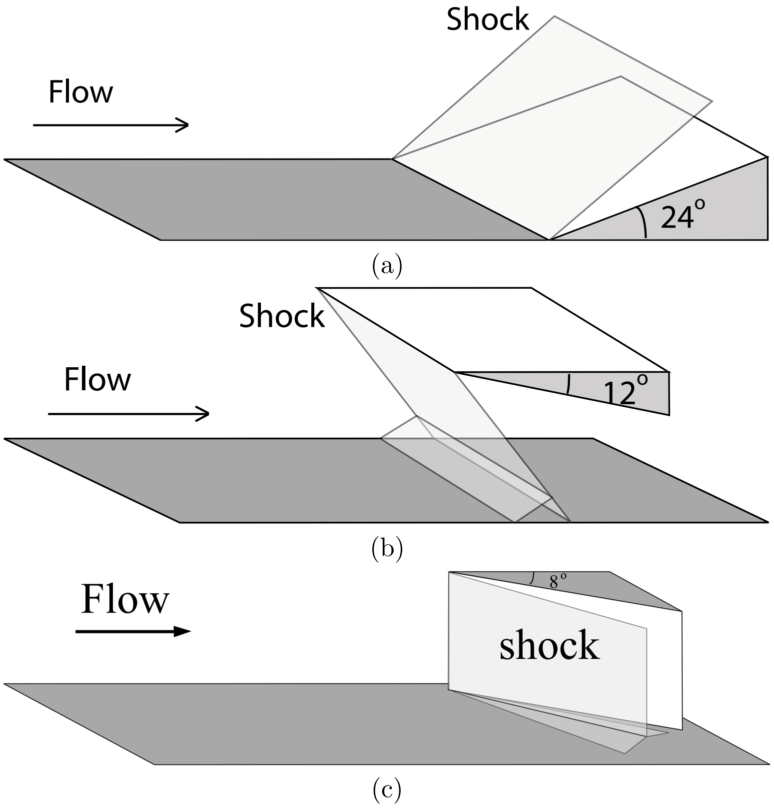

Figure 1. Configurations for the (a) compression ramp case and (b) reflected shock case, and (c) sharp-fin case.

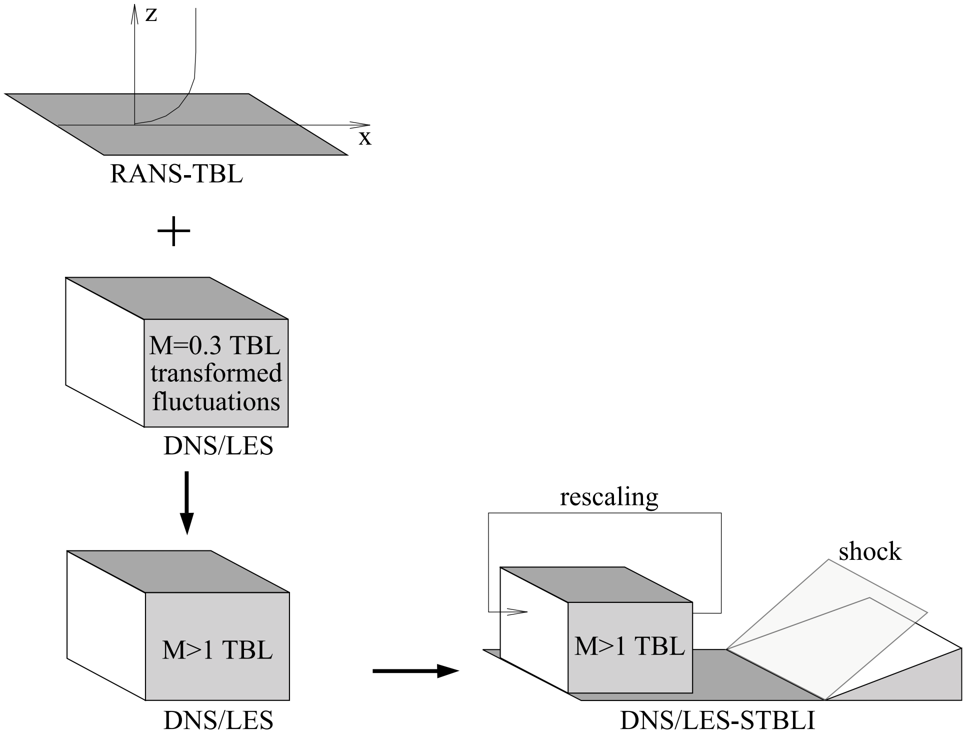

Figure 2. Initialization procedure for STBLI simulations.

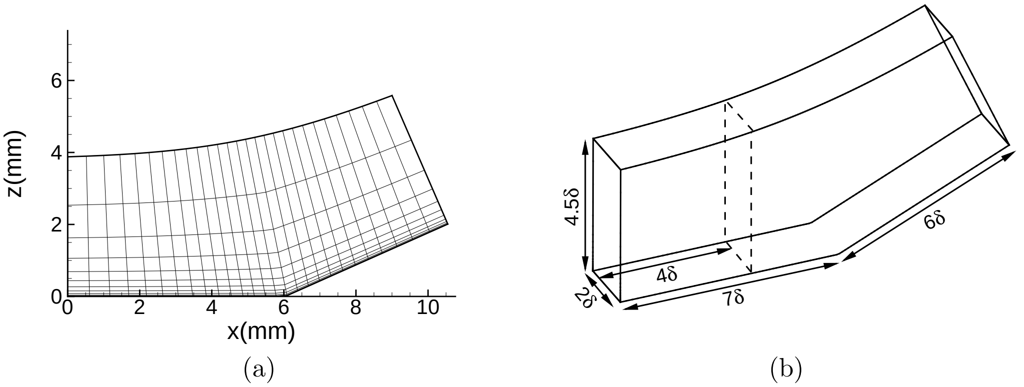

(a)

(b)

Figure 3. Computational (a) grid and (b) domain for the compression ramp case.

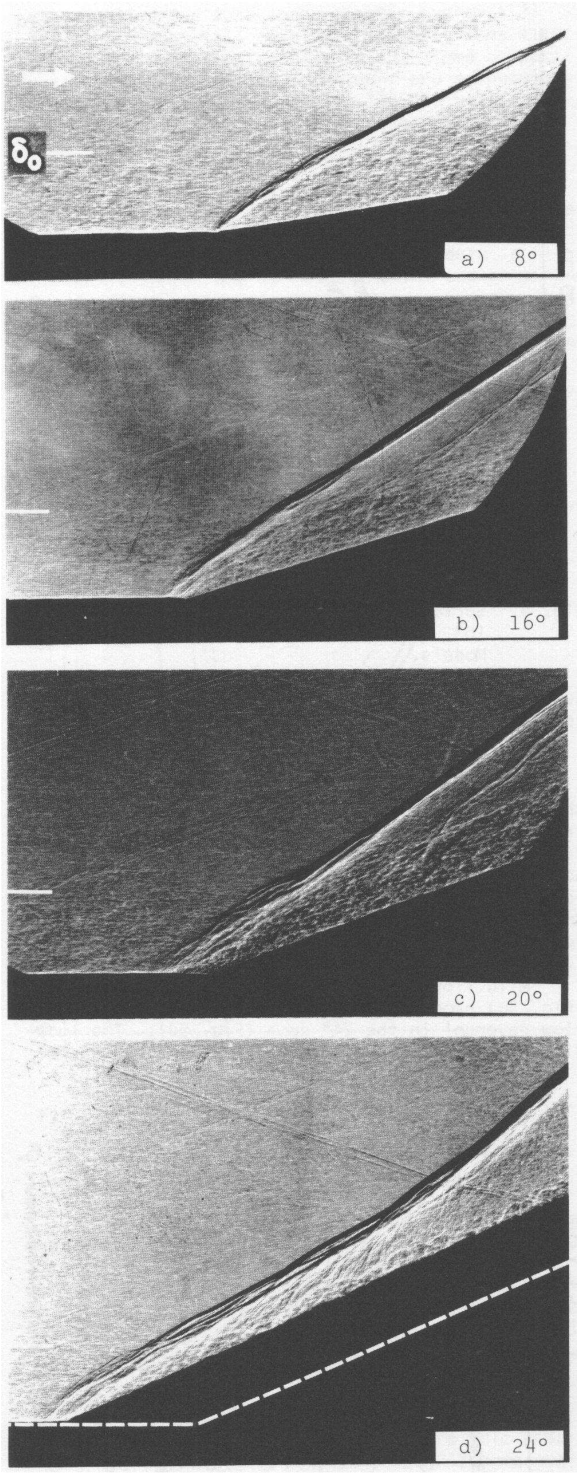

Figure 4. Shadowgraph images of Mach 2.85 compression corner interactions at various wedge angles (Settles *et al.*, 1979).

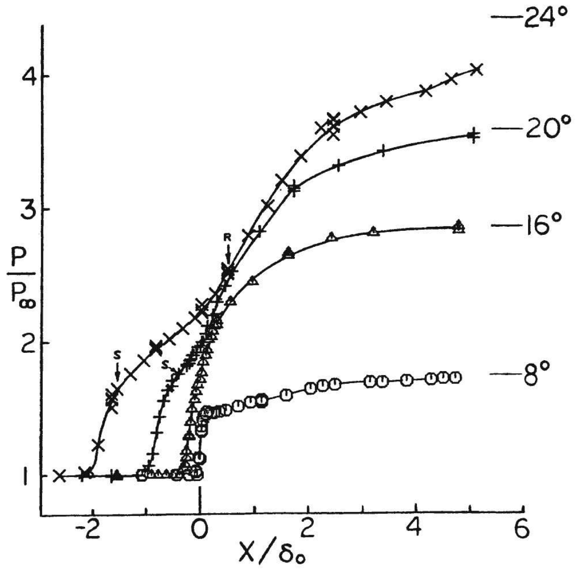

Figure 5. Surface pressure distribution on various compression corner interactions at Mach 2.85 (Settles *et al.*, 1979).

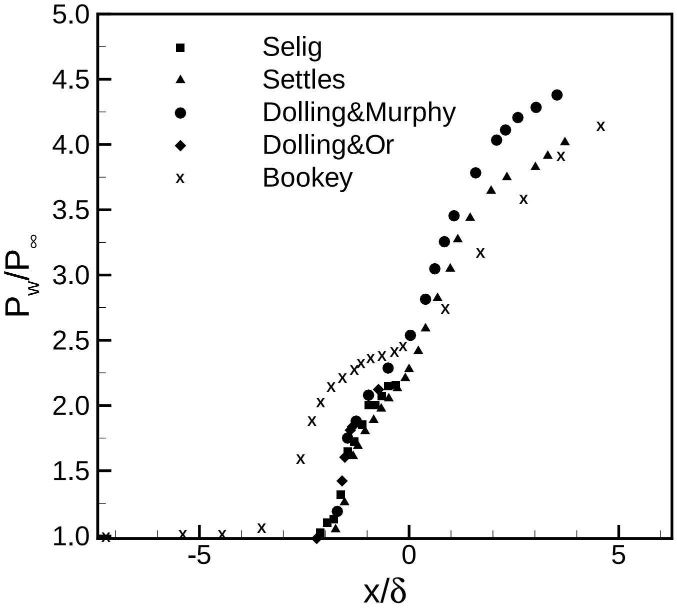

Figure 6. Wall-pressure distribution for a 24° compression corner at about Mach 3 from experimental data in the range of $Re\theta = 2400$ to about 68,000.

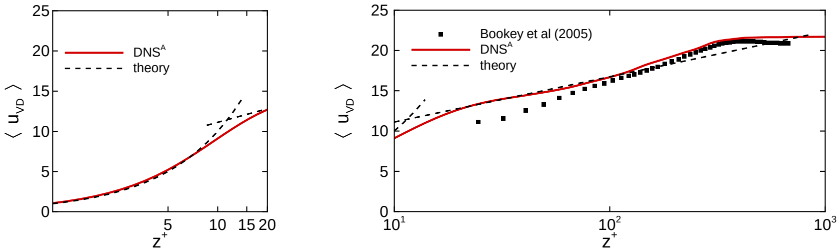

(a)

(b)

Figure 7. Comparison between the measured velocity profile[4] and the DNS data[2,3] at $Re_\theta = 2400$.

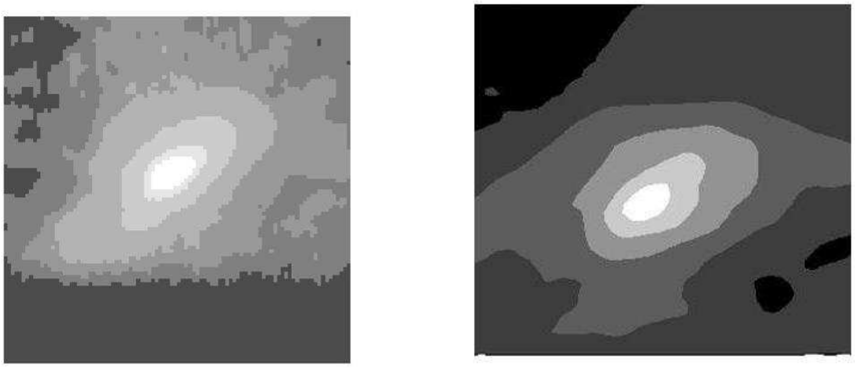

(a)

(b)

Figure 8. 2D density correlation for the incoming boundary layer, (a) experimental[4] and (a) DNS[3] data at $Re_\theta = 2400$.

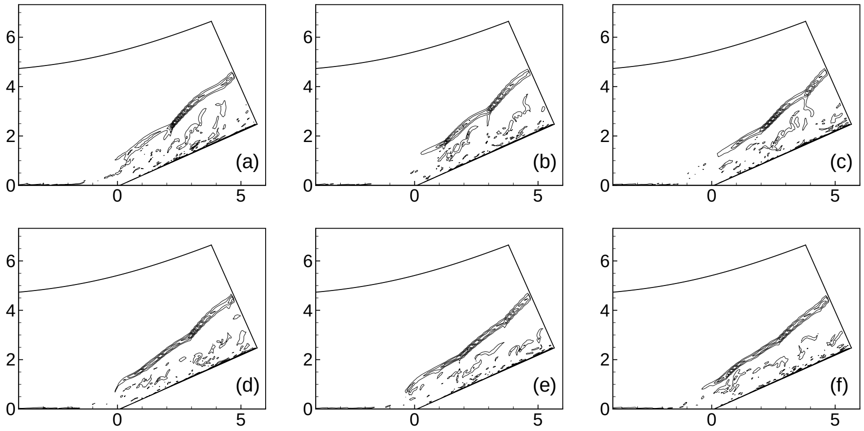

Figure 9. Sequence of $|\nabla\rho|$ contours from DNS[2,3] (coordinate unit in δ).

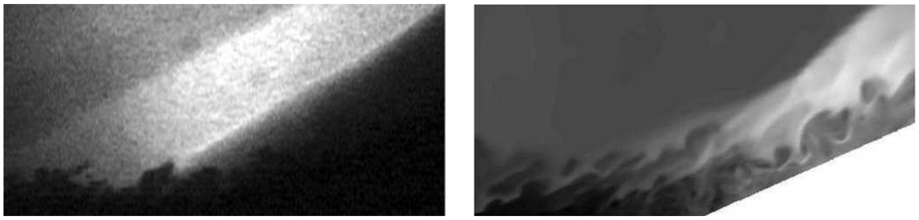

(a) (b)

Figure 10. (a) Filtered Rayleigh scattering images from experiments[4] and density contour plot from DNS.[3]

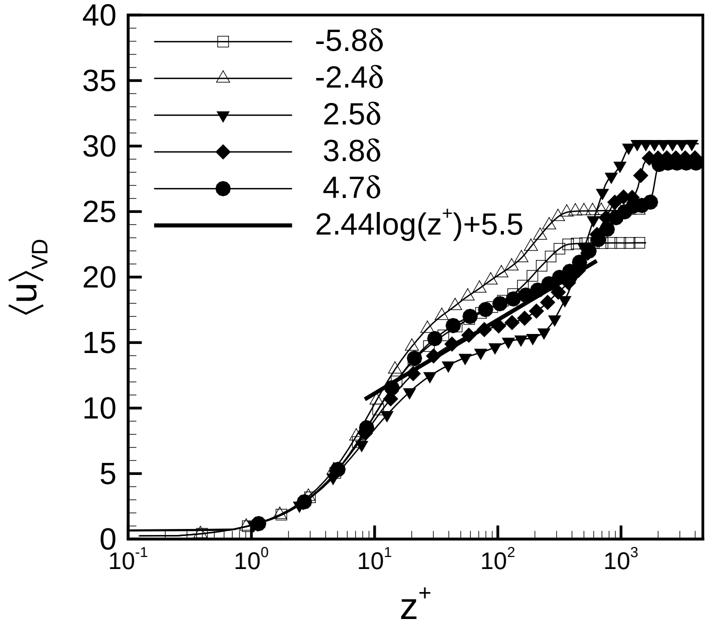

Figure 11. Van-Driest transformed velocity profile at different streamwise locations from DNS.[2,3]

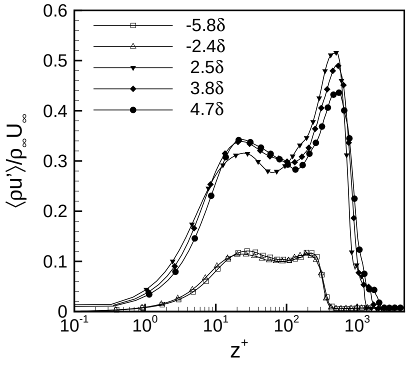

Figure 12. Mass flux turbulence intensity at different streamwise locations from DNS..[2,3]

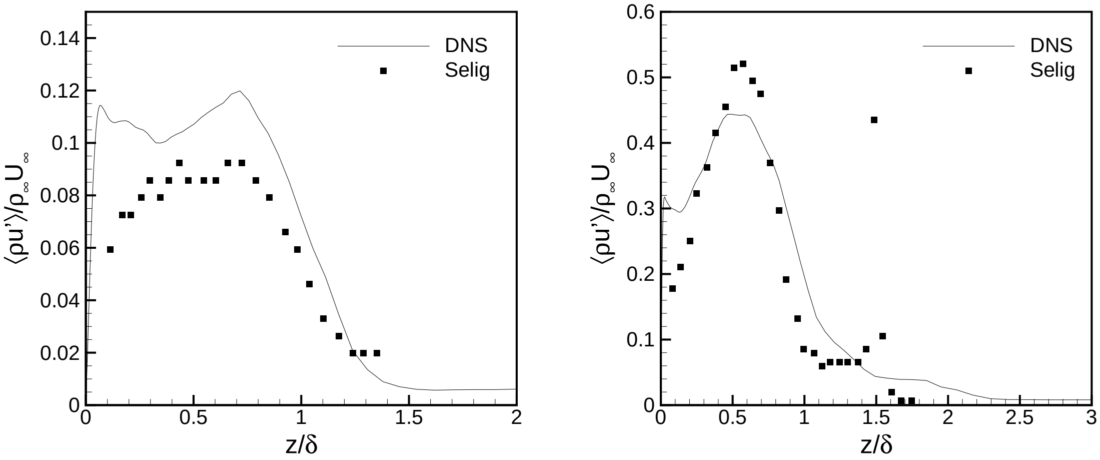

(a)

(b)

Figure 13. Comparison of the mass flux turbulence intensity for the compression ramp case upstream (a) and downstream (b) of the interaction. Experimental data from Selig.[23]

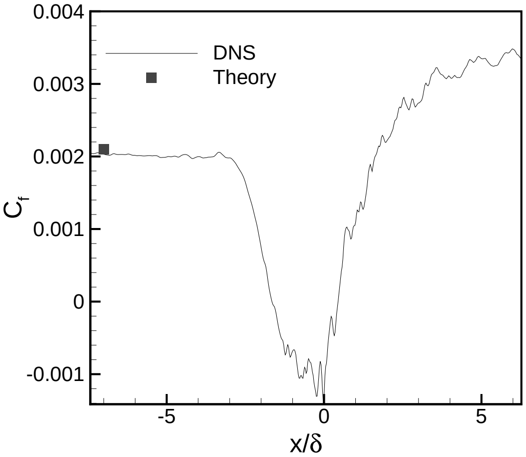

Figure 14. Skin friction coefficient from DNS.[2,3]

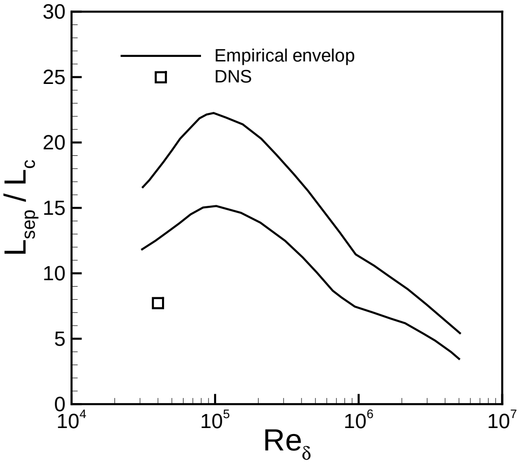

Figure 15. Correlation between separation length and Reynolds number.[24]

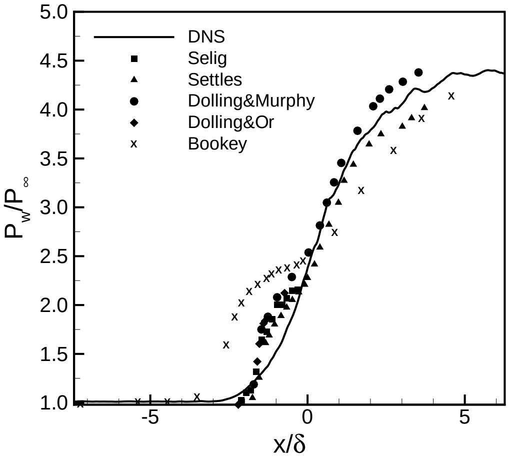

Figure 16. Wall-pressure distribution from experiments and DNS data. The experimental data are at Re_θ **of about 68,000 for Selig,[23] Settles,[20] Dolling & Murphy[15] and Dolling & Or[22] and at** $Re_\theta = 2400$ **for Bookey** *et al.*[4] **The DNS data are at** $Re_\theta = 2400$.[3]

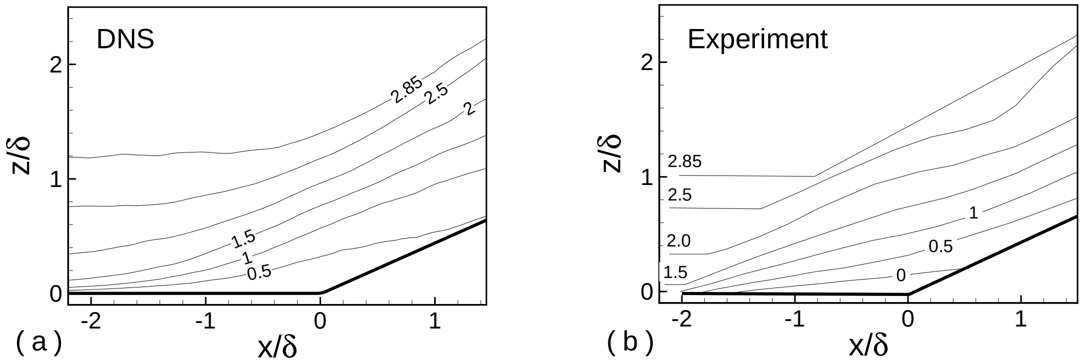

Figure 17. Time averaged contour plots of Mach number (a) DNS[3] and (b) experimental[20] data.

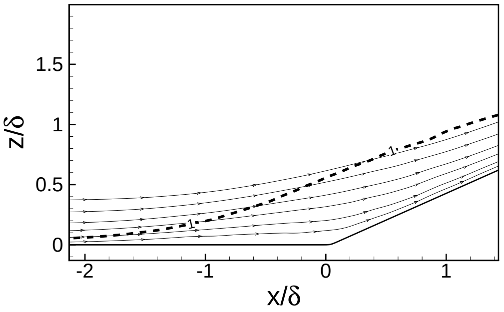

Figure 18. Streamlines and sonic line near the corner from DNS.[3]

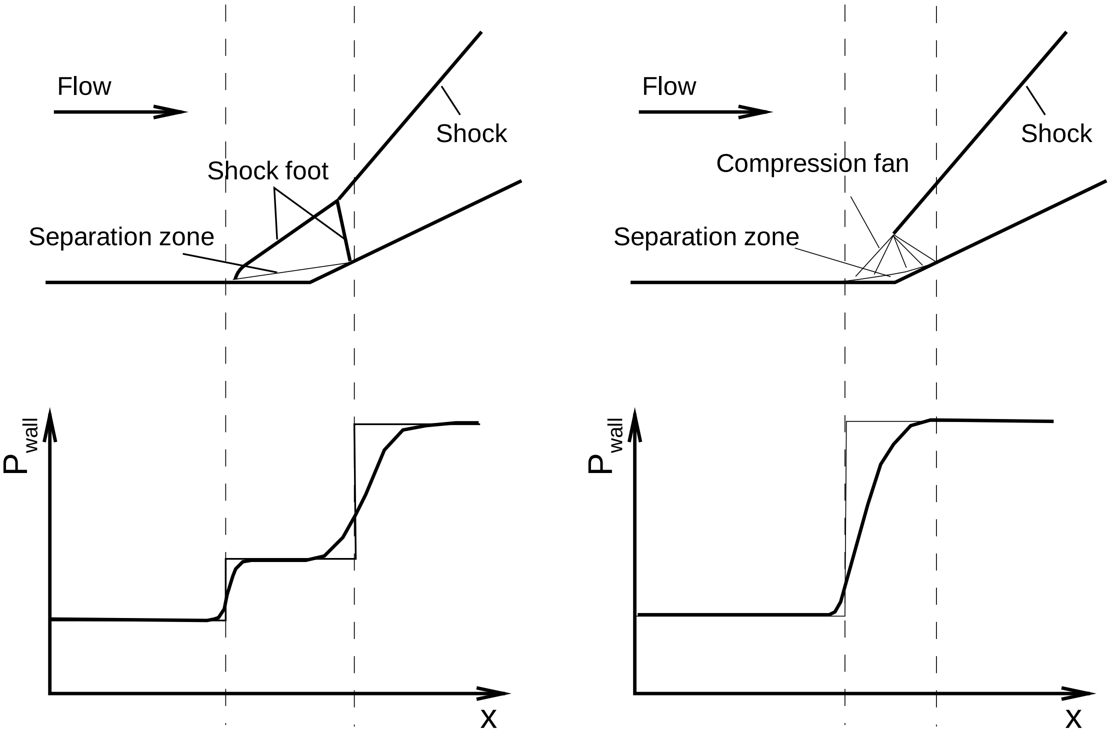

(a) (b)

Figure 19. Sketch of flow patterns in (a) experimental data and (b) DNS data.

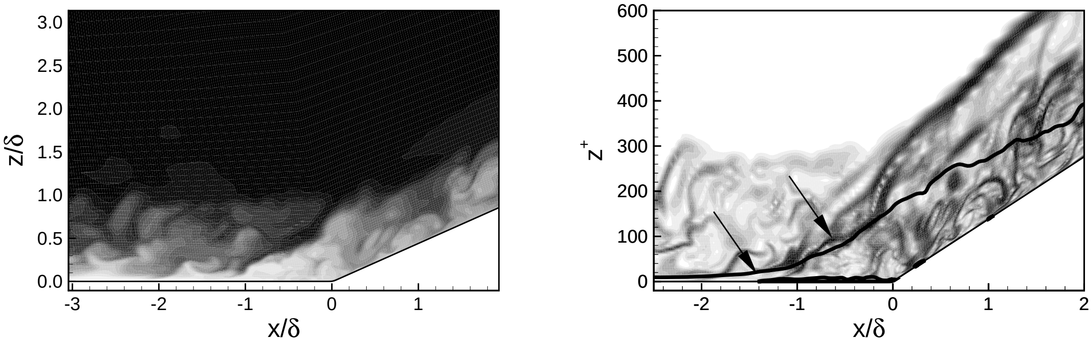

(a) (b)

Figure 20. (a) Contours of entropy and (b) numerical schlieren with Mach lines from DNS.[3] The arrows indicate the expected (upstream) and DNS shock-foot location.

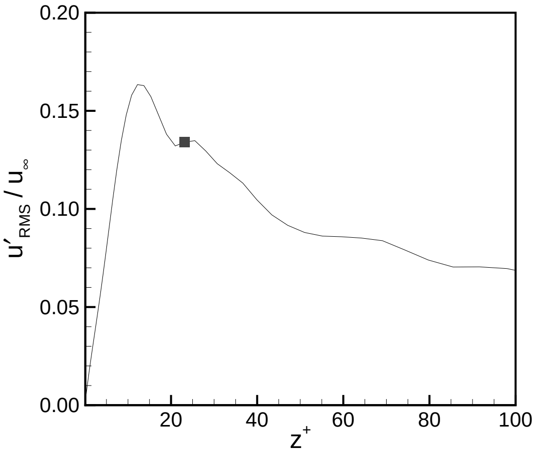

Figure 21. Profile of the normalized magnitude of velocity fluctuations at the expected shock-foot location from DNS data.[3]

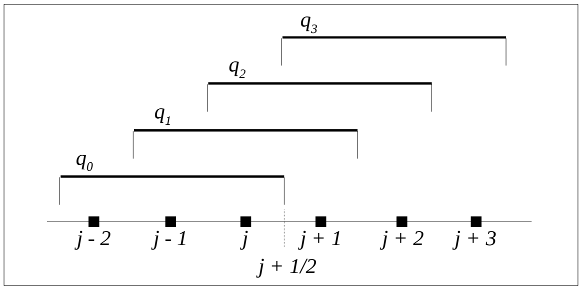

Figure 22. Sketch of the candidate stencils approximating the flux at $(i + 1/2)$ for $r = 3$ in WENO.

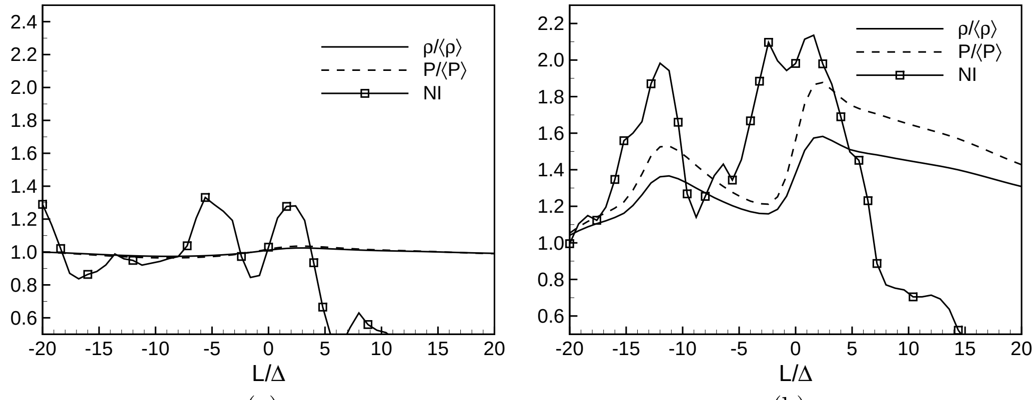

(a)

(b)

Figure 23. Density, pressure and non-linearity index across a shocklet in two-dimensional isotropic turbulence (a) $\langle M_t \rangle = 0.2$, **(b)** $\langle M_t \rangle = 0.5$.

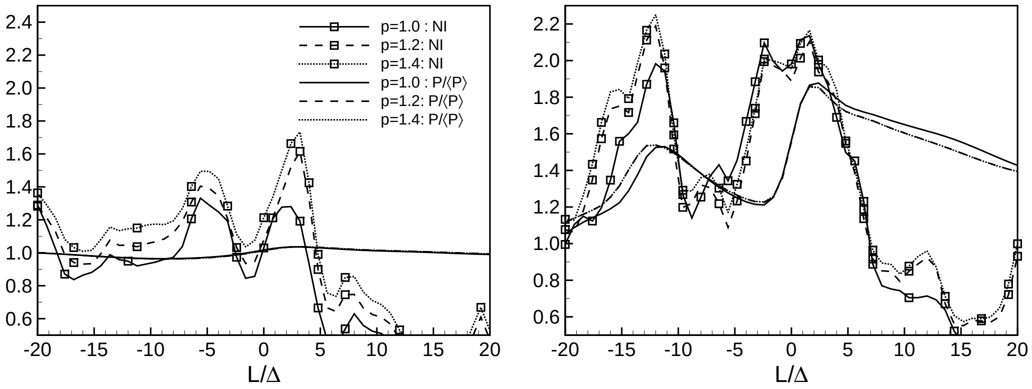

(a) (b)

Figure 24. Pressure and non-linearity index across a shocklet in two-dimensional isotropic turbulence (a) $\langle M_t \rangle = 0.2$, (b) $\langle M_t \rangle = 0.5$ for various WENO adaption sensitivities.

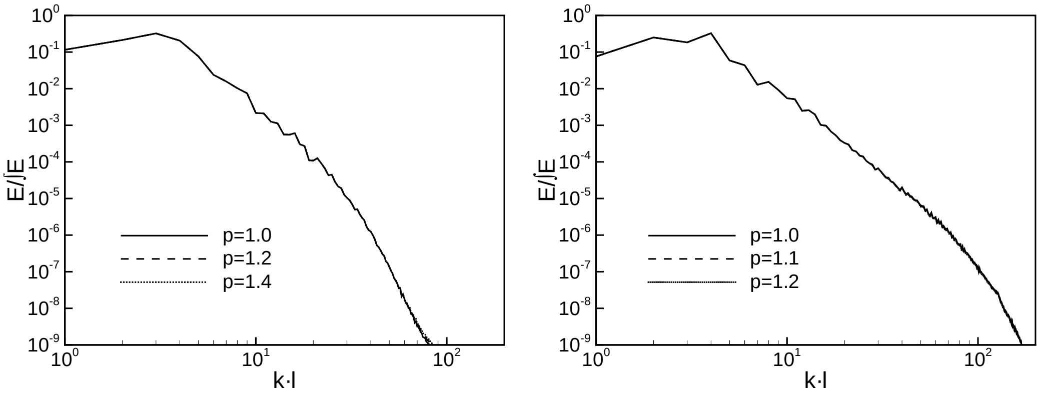

(a) (b)

Figure 25. Energy spectra in two-dimensional isotropic turbulence (a) $\langle M_t \rangle = 0.2$, (b) $\langle M_t \rangle = 0.5$ for various WENO adaption sensitivities.

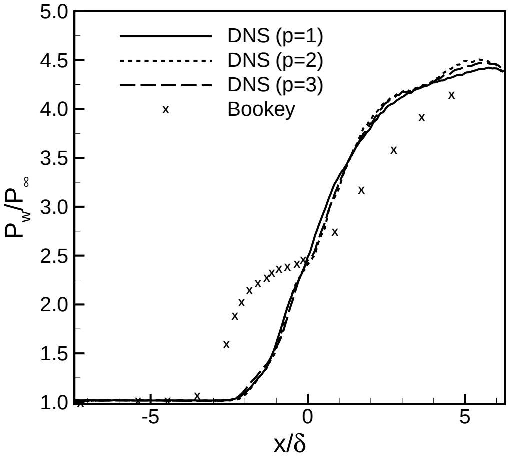

Figure 26. Wall-pressure distribution for DNS of STBLI varying p.